Energy Conversion and Management 283 (2023) 116953

Contents lists available at ScienceDirect

Energy Conversion and Management

journal homepage: www.elsevier.com/locate/enconman

Investigation of energy dissipation of an H-type vertical axis wind turbine based on entropy production theory

Qinghong Tang [a], Yuxin Wu [a,b,*], An Yu [c], Bin Peng [d], Yifu Wang [c], Junfu Lyu [a]

[a] Department of Energy and Power Engineering, Tsinghua University, Beijing 100084, China
[b] Institute for Carbon Neutrality, Tsinghua University, Beijing 100084, China
[c] College of Energy and Electrical Engineering, Hohai University, Nanjing 211100, China
[d] College of Water Conservancy and Hydropower Engineering, Hohai University, Nanjing 210098, China

ARTICLE INFO

Keywords:
Vertical axis wind turbine
Entropy production theory
Power coefficient
Wake energy loss
Energy loss coefficient

ABSTRACT

In vertical axis wind turbine (VAWT) research, amount studies have been conducted about the flow field around the blades, but the effect of blade tip vortex was not revealed clearly. The present study emphasized on the effect of blade tip vortex on energy loss in wake region and employed entropy production theory to determine where and how energy loss generates quantitatively. The numerical simulation was conducted for the VAWTs versus various tip speed ratio (TSR) conditions, and the numerical results were analyzed by entropy production method. The energy loss calculated by entropy production theory in VAWTs flows increases with TSR increasing. The distribution of entropy production rate (EPR) in wake region was asymmetrical due to the influence of blade tip vortex diffusion downstream and two fluctuation peaks appeared on EPR curves. The energy loss coefficient was defined to represent the energy deficit and kinetic energy recovery in wake region quantitatively. Generally, the energy loss coefficient was reduced to 0.1 between 8D to 9D in wake region and was equal to 0.1051 at $x = 8D$ under optimal condition TSR = 2.19. The present study can guide configuration optimization of VAWTs to improve wind energy utilization and revenue of wind farms.

1. Introduction

The exploitation of clean energy resources is the inevitable way for society to support the development of the industry. A form of clean energy, wind energy has the advantages of being sufficient, economical, renewable, and with no pollution and can be used as an alternative to fossil energy [1]. To improve the energy coefficient of VAWTs, plenty of research has been conducted about the local flow field around blades to optimize the aerodynamic performance of hydrofoils. However, the blade tip vortex was inevitable in VAWTs operation, but few studies focused on the influence of blade tip vortex on the performance of VAWTs. Moreover, wake characteristics were also important for wind turbines and wind farms and it was also important to study the energy deficit as well as kinetic energy recovery in wake region.

Plenty of achievements obtained for VAWTs focused on aerodynamic performance, control systems, dynamic stall, wake flow field through using theoretical, experimental, and numerical methods. To improve the efficiency of wind energy conversion, the aerodynamic performance of the VAWTs is the point of research. Therefore, it is worth to investigate all kinds of factors that affect the aerodynamic performances of VAWTs. Li et al. [2] studied the effects of blade numbers of VAWTs on the aerodynamic forces acting on a single blade. Li et al. [3] made the experimental measurements of the straight-bladed VAWTs with different blade pitch angle, Reynolds number as well as wind velocity, and obtained the optimal blade pitch angle and wind velocity. Zamani et al. [4] proposed a novel blade of VAWTs with porous media and found the enhancement of power and torque coefficient near optimum tip speed ratio equipped with porous media blades. Arpino et al. [5] displayed the details of VAWTs flow field by PIV (particle image velocimetry) and put forward a validation benchmark for computational fluid dynamics (CFD) models through PIV measurements. The effects of the blade tip of VAWTs on aerodynamic performance as well as flow regimes were studied by Miao et al. [6] by comparing them with twenty blade tips. As for the trailing edge of the blade, the performance of the semi-flexible trailing edge of VAWTs was measured by experiments [7]. From the point of flow control, an adaptive flap was added to the blade that can mitigate the flow separation in trailing edge region, and the effects of flap length as well as location were studied by Hao et al. [8]. Chen et al. [9] used the high-fitting neural network to predict the mean

* Corresponding author at: Department of Energy and Power Engineering, Tsinghua University, Beijing 100084, China.
E-mail address: wuyx09@mail.tsinghua.edu.cn (Y. Wu).

https://doi.org/10.1016/j.enconman.2023.116953
Received 21 January 2023; Received in revised form 16 March 2023; Accepted 19 March 2023
Available online 29 March 2023
0196-8904/© 2023 Elsevier Ltd. All rights reserved.

Nomenclature

x,y,z	Cartesian spatial coordinates m
θ	azimuth angle [°]
β	blade pitch angle [°]
H	span length [m]
C_{power}	power coefficient
u,v,w	instantaneous velocity [m/s]
$\overline{u},\overline{v},\overline{w}$	time-averaged velocity [m/s]
u',v',w'	fluctuated velocity [m/s]
ρ	density [kg/m^3]
ε	turbulent dissipation rate [m^2/s^3]
λ	tip speed ratio
k	turbulent kinetic energy [m^2/s^2]
μ	dynamic viscosity [N·s/m^2]
τ_{ij}	Reynolds stress tensor
q	heat flux [W/m^2]
T	absolute temperature [K]
Φ,Φ	dissipation functions
P_D	power loss by EPDD [W]
A_C	area of computational domain inlet [m^2]
V_C	volume of computational domain [m^3]
D	runner diameter [m]
H_C	Height of computational domain [m]
A	swept area of wind turbine [m^2]
R	rotor radius [m]
τ_W	wall shear stress [Pa]
U	free-stream wind velocity [m/s]
C_l	energy loss coefficient
ω_z	vorticity in z direction [s^{-1}]
S_D	entropy production by direct dissipation [W/K]
S_D	entropy production by turbulent dissipation [W/K]
S_D	entropy production by wall shear stress [W/K]
P_D	power loss by EPTD [W]
P_W	power loss by EPWS [W]
S	instantaneous specific entropy [J/(kg·K)]
$\overline{s}$	time-average specific entropy [J/(kg·K)]
s'	fluctuated specific entropy [J/(kg·K)]
Q	rotor torque [N·m]
ω_r	angular velocity [rad/s]

Abbreviation

EPDD	entropy production rate by direct dissipation [W/(m^3·K)]
EPTD	entropy production rate by turbulent dissipation [W/(m^3·K)]
EPWS	entropy production rate by wall shear stress [W/(m^2·K)]
EPR	entropy production rate [W/(m^2·K)]
TEPR	total entropy production rate [W/(m^2·K)]
TSR	tip speed ratio
VAWT	vertical axis wind turbine
CFD	computational fluid dynamics
LE	leading edge
TE	trailing edge

Subscripts

t	turbulent
eff	effective value
i,j,k	direction of Cartesian coordinates
Num.	numerical simulation
Exp.	experiment

TSR of VAWTs based on CFD data. Zhang et al. [10,11] proposed a novel blade with bionic airfoil and found that the power performance of bionic airfoil was improved in dynamic stall.

The published achievements in energy analysis of VAWTs were conducted toward external characteristics as well as internal characteristics. The external characteristics are the fundamental physical quantities such as torque, power coefficient, lift force, and drag force which can evaluate the performance of VAWTs macroscopically [12]. The internal characteristics were presented in the form of flow field to display the details of flow regimes and further analyze the spatial distribution of energy loss through such as velocity field, vorticity field, pressure field and vortex identification [3,13,14]. Many reports studied the flow field to reflect the energy loss of VAWTs but the flow field cannot reveal the spatial energy loss of VAWTs directly. The entropy production theory is an excellent method to calculate energy loss quantitatively in flows and can determine where and how the energy loss occurs intuitively. Mamouri et al. [15,16] used entropy production method to analyze the performance of different airfoils and studied the relation between entropy generation integral and drag coefficient. The entropy production method is an effective criterion for design, optimization of VAWTs, and evaluation as well as calculation of energy loss of VAWT flows. Soltanmohamadi et al. [17] used the entropy generation method to evaluate the performance of Wells turbine between a suggested design and a constant chord and proved the superiority of the new design with decreasing of 26.02 % in entropy generation. Nazeryan et al. [18] compared the performance of Wells turbine with a constant thickness blade and a variable thickness blade by entropy generation analysis. Ghisu et al. [19] made re-examination the mechanisms of the entropy generation in flows and analyzed the details of entropy generation in isolated airfoils as well as Wells turbines. Therefore, the exergy method was used in wind turbine to evaluate the exergy efficiency of wind turbine and energy characteristics.

Plenty of studies focused on the local flow field around blades of VAWTs and the velocity recovery in wake regions. However, the adverse flow in blade tip region also had an impact on VAWTs performance and the energy loss mechanisms in blade tip region have not been revealed clearly. The objectives of the present research are to reveal the distribution of energy loss due to blade tip in wake region and the energy loss evolution in wake region.

In this study, a numerical simulation was conducted for a VAWT with two blades versus various TSRs. This research aims to employ the entropy production theory for energy loss analysis in VAWT flows and reveal the regularity of energy dissipation in VAWT fields versus various TSRs. First of all, the validation of simulation was verified and the performance of VAWT was analyzed. Then, the entropy production in runner was calculated and the local flow field around blades was analyzed. Finally, the energy loss in blade tip wake region was revealed by entropy production method and an energy loss coefficient was defined.

2. Governing equations and entropy production theory

The RANS method was adopted in this simulation, and the governing equations are shown as follows:

$$\frac{\partial \overline{u}_i}{\partial x_i} = 0 \tag{1}$$

$$\rho\left(\frac{\partial \overline{u}_i}{\partial t} + u_j\frac{\partial \overline{u}_i}{\partial x_j}\right) = -\frac{\partial \overline{p}}{\partial x_i} + \mu\frac{\partial}{\partial x_j}\left(\frac{\partial \overline{u}_i}{\partial x_j} + \frac{\partial \overline{u}_j}{\partial x_i}\right) + \frac{\partial \tau_{ij}}{\partial x_j} \tag{2}$$

$$\tau_{ij} = -\rho\overline{u_i' u_j'} \tag{3}$$

$$-\rho\overline{u_i'u_j'} = \mu_t\left(\frac{\partial \overline{u}_i}{\partial x_j}+\frac{\partial \overline{u}_j}{\partial x_i}\right)-\frac{2}{3}\mu_t\frac{\partial \overline{u}_k}{\partial x_k}\delta_{ij}-\frac{2}{3}\rho k\delta_{ij} \tag{4}$$

where $\overline{u}$ is time-averaged velocity [m/s], t is time [s], ρ is density [kg/m^3], $\overline{p}$ is average pressure [Pa], μ is molecular dynamic viscosity [N·s/m^2] and μ_t is the eddy viscosity [N·s/m^2], τ_{ij} is Reynolds stress tensor [Pa],

δ_{ij} is the Kronecker delta operator. The subscripts (i, j, k) represent three directions in Cartesian coordinates.

From the perspective of thermodynamic system, the freestream wind undergoes the VAWT where the partial kinetic energy converts into mechanical energy. This energy conversion process is an irreversible thermodynamic process that leads to entropy generation inevitably based on the second law of thermodynamics. The entropy generation corresponds to the exergy loss can be used to calculate energy loss in VAWT flows quantitatively. The entropy transport equation in incompressible flows is shown as follows [20]:

$$\rho\left(\frac{\partial s}{\partial t}+u\frac{\partial s}{\partial x}+v\frac{\partial s}{\partial y}+w\frac{\partial s}{\partial z}\right) = -div\left(\frac{\vec{q}}{T}\right)+\frac{\Phi}{T}+\frac{\Phi_\Theta}{T^2} \tag{5}$$

where u, v and w are instantaneous velocity, s is specific entropy per unit mass [J/(kg·K)], q is heat flux [W/m^2], T is local temperature [K], Φ and Φ_Θ are dissipation function.

Based on the Reynolds time-average method, the instantaneous variables can be divided into time-average part as well as fluctuating part:

$$s = \overline{s}+s' \tag{6}$$

$$u = \overline{u}+u' \tag{7}$$

where $\overline{s}$ is time-average specific entropy, s' is fluctuating specific entropy, u' is fluctuating velocity.

Employ Reynolds time-average method, the Eq. (5) can be transformed into follows [20]:

$$\rho\left[\left(\frac{\partial \overline{s}}{\partial t}+\overline{u}\frac{\partial \overline{s}}{\partial x}+\overline{v}\frac{\partial \overline{s}}{\partial y}+\overline{w}\frac{\partial \overline{s}}{\partial z}\right)+\left(\frac{\partial \overline{u's'}}{\partial x}+\frac{\partial \overline{v's'}}{\partial y}+\frac{\partial \overline{w's'}}{\partial z}\right)\right] = -div\left(\overline{\frac{\vec{q}}{T}}\right)+\underbrace{\overline{\frac{\Phi}{T}}}_{I}+\underbrace{\frac{\overline{\Phi_\Theta}}{T^2}}_{II} \tag{8}$$

where in the right side of Eq. (8), the dissipation function term I represents the EPR induced by fluid viscosity effects and the dissipation function term II represents the EPR induced by heat transfer irreversibility. The temperature variation in VAWT flows is negligible so that the thermodynamic system was treated as constant temperature system.

The dissipation function term I can be written as follows [20]:

$$\frac{\Phi}{T} = \frac{\mu}{T}\left[\begin{array}{c} 2\left\{\left(\frac{\partial u}{\partial x}\right)^2+\left(\frac{\partial v}{\partial y}\right)^2+\left(\frac{\partial w}{\partial z}\right)^2\right\} \\ +\left(\frac{\partial u}{\partial y}+\frac{\partial v}{\partial x}\right)^2+\left(\frac{\partial u}{\partial z}+\frac{\partial w}{\partial x}\right)^2+\left(\frac{\partial v}{\partial z}+\frac{\partial w}{\partial y}\right)^2 \end{array}\right] \tag{9}$$

Employ Reynolds time-average method, Eq. (9) can be written as Eq. (10) and can be divided into time-average part (Eq. (11)) as well as fluctuating part (Eq. (12)) [20]:

$$\overline{\frac{\Phi}{T}} = \frac{\mu}{T}\left[\begin{array}{c} 2\left\{\left(\frac{\partial \overline{u}}{\partial x}\right)^2+\left(\frac{\partial \overline{v}}{\partial y}\right)^2+\left(\frac{\partial \overline{w}}{\partial z}\right)^2\right\}+\left(\frac{\partial \overline{u}}{\partial y}+\frac{\partial \overline{v}}{\partial x}\right)^2+\left(\frac{\partial \overline{u}}{\partial z}+\frac{\partial \overline{w}}{\partial x}\right)^2+\left(\frac{\partial \overline{v}}{\partial z}+\frac{\partial \overline{w}}{\partial y}\right)^2+ \\ 2\left\{\left(\frac{\partial u'}{\partial x}\right)^2+\left(\frac{\partial v'}{\partial y}\right)^2+\left(\frac{\partial w'}{\partial z}\right)^2\right\}+\left(\frac{\partial u'}{\partial y}+\frac{\partial v'}{\partial x}\right)^2+\left(\frac{\partial u'}{\partial z}+\frac{\partial w'}{\partial x}\right)^2+\left(\frac{\partial v'}{\partial z}+\frac{\partial w'}{\partial y}\right)^2 \end{array}\right] \tag{10}$$

$$\dot{S}_{\overline{D}}''' = \frac{\mu_{eff}}{T}\left[\begin{array}{c} 2\left\{\left(\frac{\partial \overline{u}}{\partial x}\right)^2+\left(\frac{\partial \overline{v}}{\partial y}\right)^2+\left(\frac{\partial \overline{w}}{\partial z}\right)^2\right\} \\ +\left(\frac{\partial \overline{u}}{\partial y}+\frac{\partial \overline{v}}{\partial x}\right)^2+\left(\frac{\partial \overline{u}}{\partial z}+\frac{\partial \overline{w}}{\partial x}\right)^2+\left(\frac{\partial \overline{v}}{\partial z}+\frac{\partial \overline{w}}{\partial y}\right)^2 \end{array}\right] \tag{11}$$

$$\dot{S}_{D'}''' = \frac{\mu_{eff}}{T}\left[\begin{array}{c} 2\left\{\left(\frac{\partial u'}{\partial x}\right)^2+\left(\frac{\partial v'}{\partial y}\right)^2+\left(\frac{\partial w'}{\partial z}\right)^2\right\} \\ +\left(\frac{\partial u'}{\partial y}+\frac{\partial v'}{\partial x}\right)^2+\left(\frac{\partial u'}{\partial z}+\frac{\partial w'}{\partial x}\right)^2+\left(\frac{\partial v'}{\partial z}+\frac{\partial w'}{\partial y}\right)^2 \end{array}\right] \tag{12}$$

$$\mu_{eff} = \mu+\mu_t \tag{13}$$

where $\dot{S}_{\overline{D}}'''$ is the entropy production rate by direct dissipation (EPDD) [W/(m^3·K)], which is induced by time-averaged velocity, $\dot{S}_{D'}'''$ is the entropy production rate by turbulent dissipation (EPTD) [W/(m^3·K)], which is induced by fluctuating velocity.

However, in Reynolds time-average method, the fluctuating velocity is not calculated directly so that the EPTD was identified by approximation function coupling with turbulence model. As for k-ω turbulence model, the EPDD can be calculated by the function as follows [21,22]:

$$\dot{S}''_{D'} = 0.09\frac{\rho\omega k}{T} \tag{14}$$

where ω is turbulent eddy frequency [s^{-1}], 0.09 is constant [23,24], k is turbulent kinetic energy [m^2/s^2].

The wall function proposed by Duan et al. [25,26] to calculate entropy production rate by wall shear (EPWS) is shown as follows:

$$S'_w = \frac{\tau_w\cdot v_w}{T} \tag{15}$$

where τ_w is wall shear stress [Pa], and v_w is first grid cell velocity near wall [Pa].

The entropy production can be obtained by EPR integrating with the computational domain.

$$S_{\overline{D}} = \int_V \dot{S}_{\overline{D}}'''\,dVS_{D'} = \int_V \dot{S}_{D'}'''\,dVS_W = \int_A \dot{S}_W''\,dA \tag{16}$$

where $S_{\overline{D}}$ is entropy production by direct dissipation [W/K], $S_{D'}$ is entropy production by turbulent dissipation [W/K], S_W is entropy production by wall shear stress [W/K].

The power loss can be written as follows:

$$P_{\overline{D}} = T\cdot S_{\overline{D}}P_{D'} = T\cdot S_{D'}P_W = T\cdot S_W \tag{17}$$

where $P_{\overline{D}}$ is the power loss by direct dissipation [W], $P_{D'}$ is the power loss by turbulent dissipation [W], P_W is the power loss by wall shear stress [W].

Therefore, the total entropy production and the total power loss can be written as follows:

$$P_{Total} = P_{\overline{D}}+P_{D'}+P_W \tag{18}$$

$$S_{Total} = S_{\overline{D}}+S_{D'}+S_W \tag{19}$$

According to the theory mentioned before, the energy loss can be

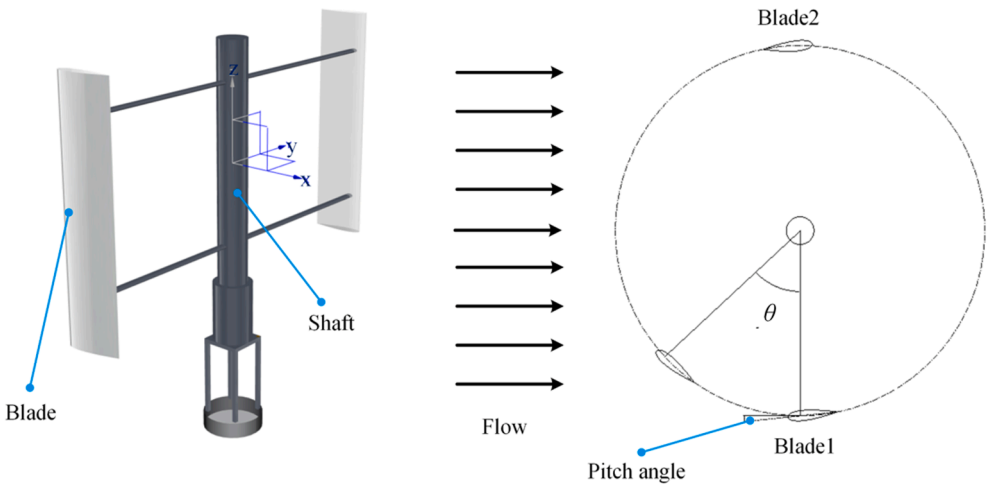

Fig. 1. H-type VAWT structure.

obtained by integration quantitatively and the spatial distribution of energy loss can be captured by entropy production method.

3. Geometric model and numerical method

3.1. VAWT model

This simulation was conducted to reveal the energy dissipation details of an H-type VAWT based on experiments by Li et al. [3]. The H-type VAWT model was shown in Fig. 1 and was composed of wind blades, generator, shaft, and other auxiliary equipment. The geometric parameters in this simulation were consistent with experiment VAWT model [3] and the specific parameters were listed in Table 1. The VAWT contains two straight blades with a symmetric airfoil profile NACA0021 and the chord length is 0.265 m. The rotor diameter is $D = 2$ m and the blade height of the VAWT is $H = 1.2$ m. The blade pitch angle was set at $\beta = 6^\circ$ because the VAWT can achieve maximum power coefficient by experimental validation [3].

The performance of wind turbine was defined by power coefficient whose expression is shown as follows:

$$C_{power} = \frac{Q\omega_r}{0.5\rho A U_\infty^3} \tag{20}$$

where C_{power} is the power coefficient, Q is rotor torque, ω_r is angular velocity of VAWT, ρ is air density, $A = DH$ represents the swept area of wind turbine, U_∞ is the free-stream wind velocity.

The TSR is defined as:

$$\lambda = \frac{R\omega_r}{U_\infty} \tag{21}$$

where λ is TSR, R is rotor radius.

3.2. Computational domain and mesh independence

The three-dimensional CFD approach was conducted for the simulation of VAWT flows versus various TSRs through the software ANSYS CFX and contrasted with experimental data to reveal the energy dissipation details in VAWT flows [3]. The computational domain was shown in Fig. 2, which contains rotating inner domain and static outer domain. The origin of the coordinate system is located at the center of the inner domain. As shown in Fig. 2, the length of the computation domain is $20D = 40$ m, and the width of the computation domain is c = 20 m, and the height of the computation domain is $1.2D = 2.4$ m [11,14]. As for the rotating inner domain, the rotating domain has a distance of $5D$ with the inlet and $15D$ with the outlet, $5D$ in front of the back boundary, $5D$ behind the front boundary, $1H$ above bottom boundary, $1H$ below the upper boundary. The diameter of the rotating domain is $1.2D = 2.4$ m and the height is equal to the blade height 1.2 m.

The boundary condition has a significant effect on the convergence, as shown in Fig. 2, velocity inlet was set at the inlet of computation domain, and the pressure outlet was set at outlet of domain outlet. The symmetry condition was selected on upper, bottom, front and back surfaces of computational domain and no-slip condition was set on blades as well as shaft walls.

According to the experiments, the freestream wind velocity was 8 m/s and the outlet pressure was set at a relative value with 0 Pa. In VAWT simulation, the shear stress transport (SST) k-ω was widely adopted in recent studies [10,11,14] so that SST k-ω was employed for simulations under all conditions. As for the unsteady simulation, the time step was set as the time scale in which the wind turbine rotor rotates per 1° to balance the computational resource consumption and numerical accuracy. And the validation of the time step in which VAWT rotates by 1° was verified by Zhang et al. [10].

To adjust the shape of the blade surface, the mesh was hexa-structured and generated by ANSYS ICEM. As shown in Fig. 3, the rotating inner domain was refined entirely and especially further refined in the surrounding region of straight blades. Considering the significant gradient in the boundary layer near wall, prismatic layer was generated around blades. The computational domain was split into 5.35 million elements with inner rotating domain 2.41 million elements as well as outer domain 2.94 million elements. Under this mesh strategy, the calculation was conducted and the distribution of y^+ was shown in Fig. 4. It can be seen that the y^+ has a large value in leading edge (LE) region of VAWT blades due to flow separation and the region of trailing edge (TE) is small than LE area. But the value of y^+ of entire blade wall was controlled below 3.17 approximately and most area was controlled below 1.0, which meets the requirement of viscous sub-layer ($y^+ > 5$). Therefore, this mesh scheme achieves the requirement of SST k-ω turbulence model and it is reasonable and acceptable for resolution in this simulation.

Table 1
Parameters of H-type VAWT.

Parameter	Value
Blade airfoil	NACA0021
Blade number	2
Chord length [m]	0.265
Span length H[m]	1.2
Rotor diameter D[m]	2.0
Pitch angle β[°]	6

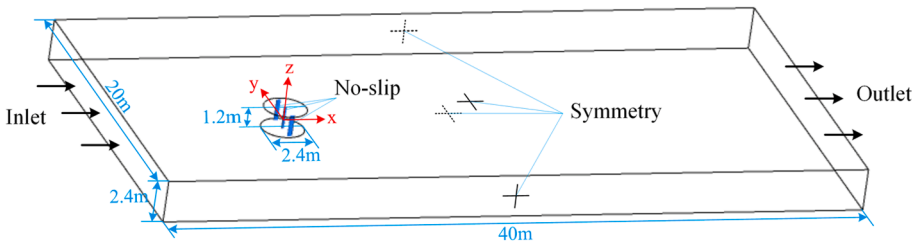

Fig. 2. Computational domain.

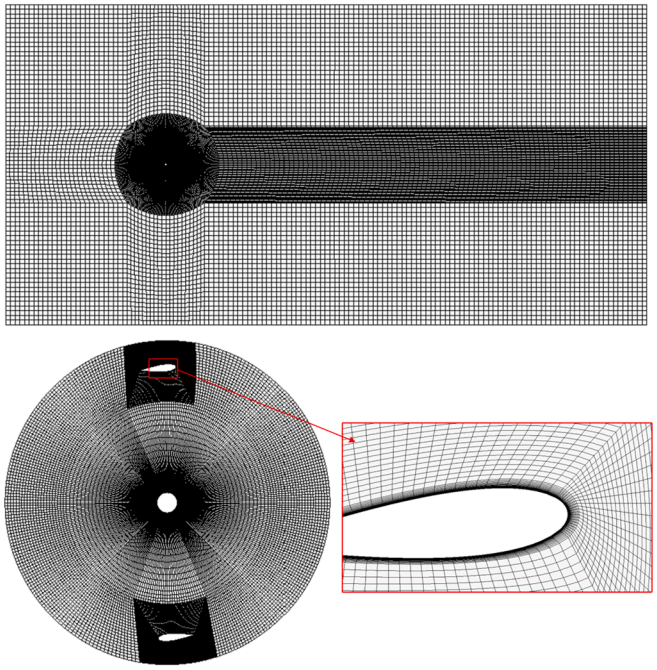

Fig. 3. Mesh grids of computational domain.

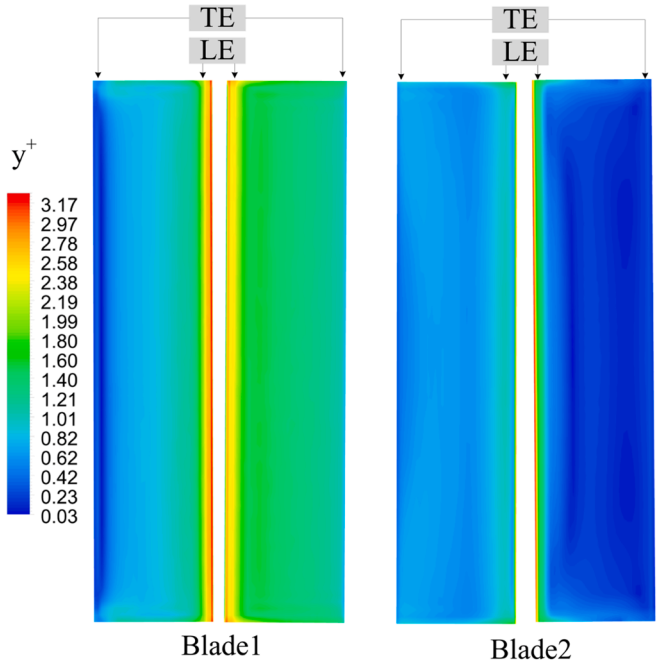

Fig. 4. The distribution of y^+ on VAWT blade wall.

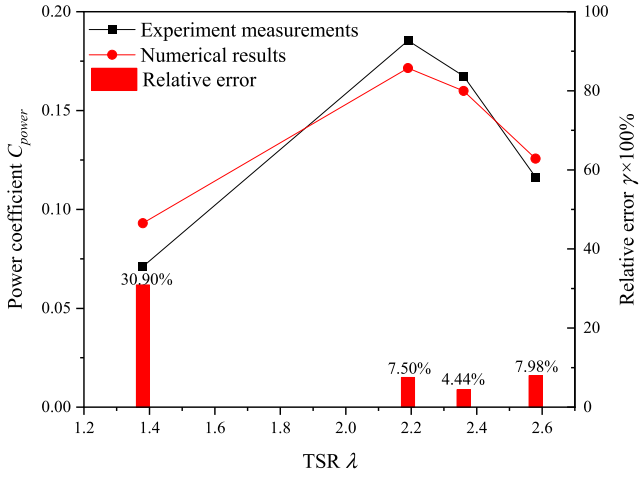

Fig. 5. Comparison of experimental measurements and numerical results for power coefficients C_{power} versus TSR conditions.

4. Results and discussions

4.1. Numerical validation

The fundamental variable power coefficient C_{power} of VAWT was selected to make the comparison between experimental and numerical results. Fig. 5 displayed the power coefficient C_{power} of the VAWT versus various TSR conditions and general agreement between numerical simulation and experimental measurements were obtained. The largest deviation between experimental measurements and numerical results appeared on $\lambda = 1.38$ condition with a relative error of 30.90 % for power coefficient. In addition, the relative error of other conditions to experimental value was less than 8 % where relative error was calculated by Eq. (22). The difference between experiments and simulations were affected by geometric model simplification, RANS method, mesh quality. However, the deviation of this simulation was acceptable and this numerical framework was credible.

$$\gamma = \frac{\left|C_{power,Exp.} - C_{power,Num.}\right|}{C_{power,Exp.}} \tag{22}$$

4.2. Analysis of energy loss in runner

The local flow field around blades can reflect the aerodynamic and stall performances of VAWTs. And the VAWT has different aerodynamic performances under different operating conditions. In this study, four TSR conditions were conducted numerically and the local vorticity field around Blade1 on the middle section ($z = 0$m) in one rotation cycle was shown in Fig. 6. At the upstream region ($0° < \theta < 180°$), the attached vortex near blade surface occupied the main part of vorticity and the detached vortex mostly appeared in blade trailing region. The detached vortex under $\lambda = 1.38$ condition was more intense than other TSR conditions. In velocity triangle, the little tangential velocity resulted in a

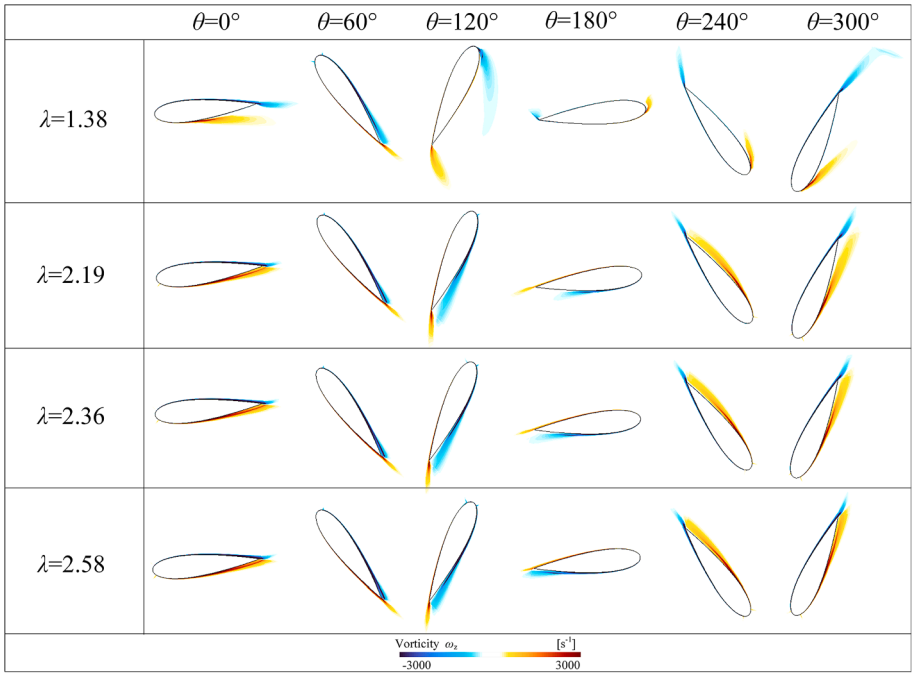

Fig. 6. Vorticity field ω_z around Blade1 middle section in one cycle versus different TSR conditions.

large angle between relative velocity and absolute velocity, which induced large flow separation on suction side of blades under $\lambda = 1.38$ condition. Among all of TSR conditions, the area as well as intensity of vorticity under $\lambda = 2.19$ condition was little than other TSR conditions and the VAWT had the maximum energy coefficient under $\lambda = 2.19$ condition. It can be concluded that the local distribution of vorticity had significant effect on rotation region and it affected the output power of runner directly. However, the influence of local field around blade on wake region of VAWTs was also worth exploring.

To study the energy loss in runner of VAWTs, Fig. 7 gave the energy loss calculated by entropy production theory and the proportion of energy loss contributed by entropy production terms EPWS, EPTD, and EPDD. It can be concluded from Fig. 7 that energy loss keeps increasing with TSR value rising from 1.38 to 2.58. The interpretation of this result is that the speed of impeller becomes larger under a high value of TSR condition, and in velocity triangle analysis the increase of tangential

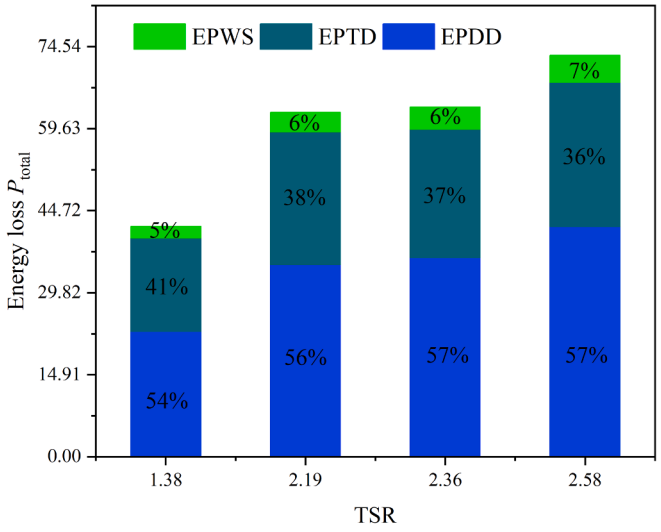

Fig. 7. The distribution of three different entropy production terms in runner versus various TSR conditions.

velocity caused an increase of relative velocity and further induce velocity shear as well as vorticity and the adverse flow caused significant energy loss. As shown in Fig. 6, the vorticity field varied from vorticity separation to attached vorticity near blade wall with TSR increasing, which meant that a more severe shear effect on blade wall appeared under higher TSR condition. So that the proportion of EPWS increased with TSR increasing and which meant energy loss due to wall shear effect increased. Among all the entropy production rate terms, the EPDD is the largest one than EPTD and EPWS versus any TSR condition. This indicated that time-averaged velocity gradients made a major contribution to energy loss in VAWT flows. And the EPWS has the least proportion of total entropy production rate (TEPR) compared with EPDD and EPTD for four TSR conditions.

Fig. 8 compared the torque of single blade and wall energy loss of single-blade induced by EPWS versus four TSRs for azimuth angle from $\theta = 0°$ to $\theta = 360°$. The energy loss near blade wall was induced by wall friction. The energy loss P_W in Fig. 8 was calculated by Eq. (17). It can be seen that the energy loss curve decreased entirely from $\theta = 0°$ to $\theta = 180°$ and grew from $\theta = 180°$ to $\theta = 360°$. The torque curve increased to its maximum value approximately at $\theta = 90°$ and then decreases. Generally, the level of energy loss became larger with TSR increasing, which kept the same trend as blade torque curve. At low TSR ($\lambda = 1.38$) condition, the trend of energy loss curve was different from other conditions where the energy loss has little growth before 90°. It was because the flow separation appeared earlier than other conditions (as shown in Fig. 6 $\theta = 0°$) and then changed into attached vorticity flow (as shown in Fig. 6 $\theta = 60°$) and flow separation induced more energy loss. The minimum value of energy loss P_W appears at about $\theta = 180°$ where blade torque curve reached to local minimum approximately. This can also be verified from Fig. 6 that the local vorticity weakened to its minimum value at $\theta = 180°$ compared with other azimuth angles. And at this azimuth angle $\theta = 180°$ the blade cannot generate positive torque for VAWT.

4.3. Analysis of energy loss in wake region

As mentioned before, the local vorticity field around blades had a significant influence on rotation domain. Further to reveal the inducements of energy loss in wake region of VAWTs, Figs. 9-12 displayed

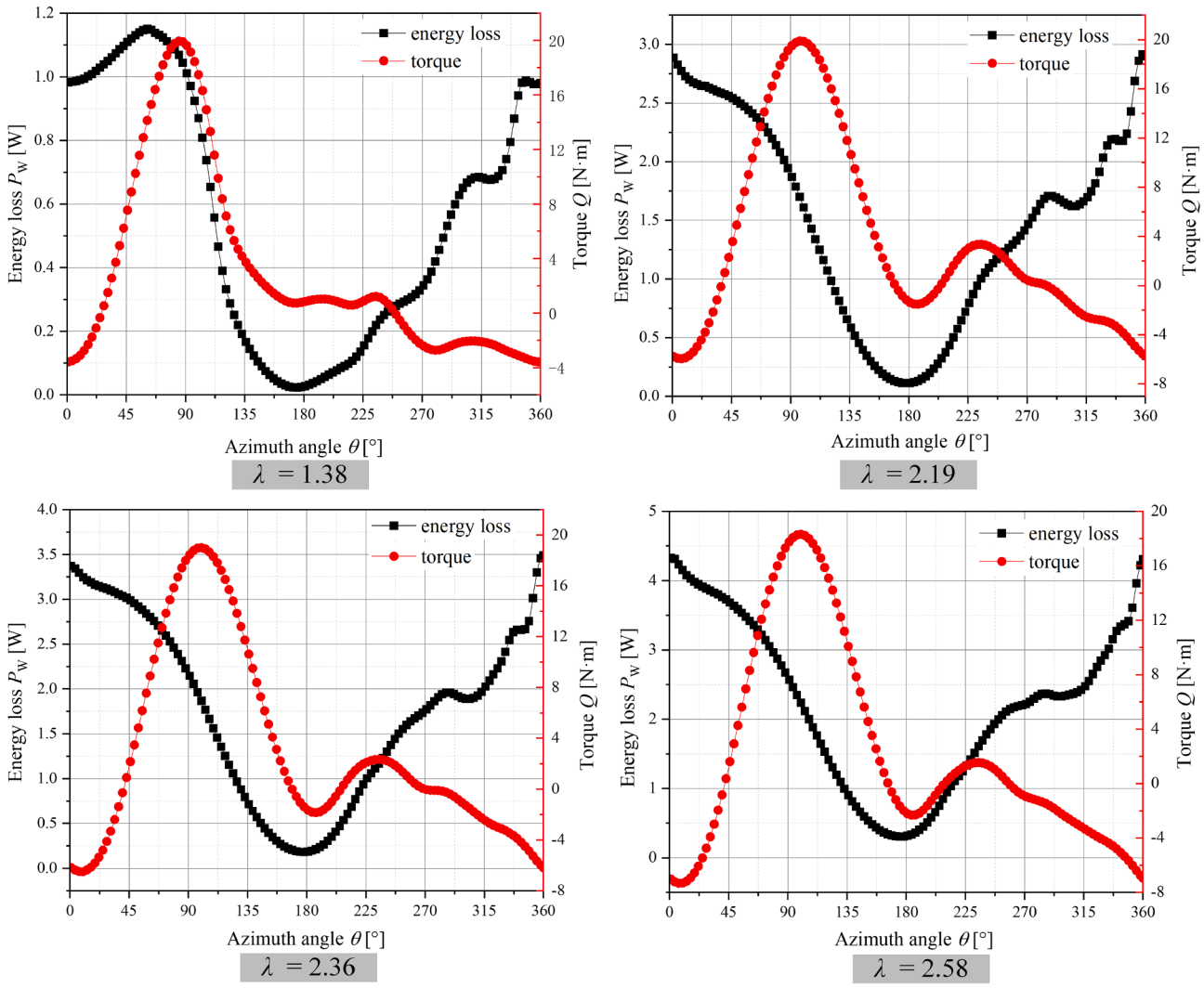

Fig. 8. The distributions of single blade wall energy loss as well as single-blade torque versus various TSR conditions.

the local EPR (EPDD and EPTD) on the YZ plane from $x = 1D$ to $x = 10D$ in one rotation cycle T_c, and the vortex structure identified by Q-criterion was also shown in Figs. 9-12. The entropy production theory can calculate the energy loss directly in the fluid domain and the distribution of EPR revealed the energy loss in wake region of VAWT directly. Generally, the strength of EPR in wake region increased with TSR increasing and the area of EPR also expanded as TSR increased, which meant that the large TSR induced a large amount of energy loss. The energy loss in wake region was mainly caused by detached vortex as well as blade tip vortex generating near blades. It can be found from Figs. 9-12 that high-level EPR mainly appeared in top and bottom region on YZ plane and the location was corresponding to blade tip in runner. So that the blade tip vortex originating from blade tips was the dominant inducement to cause high-level EPR in wake region. And the detached vortex originating from blade surface has a lighter effect than blade tip vortex on energy loss in wake region. Zhang et al. [14] and Lei et al. [27] also captured the blade tip vortex by Q-criterion in their research and length of blade tip vortex was longer than the detached or attached vortex, whose results were consistent with this research. The intense blade tip vortices occurring in blade tip induced significant energy loss in wake region. And the EPR kept strong in wake region before $x = 7D$ under four TSR conditions.

It can be concluded that the distribution of EPR in wake region was asymmetrical toward the z axis of YZ plane. It can be seen that the EPR occurred mainly on the front side of YZ planes from $x = 1D$ to $x = 10D$. This can be interpreted from the perspective of vortex dynamics. From the vortex identified by Q-criterion in Fig. 9-Fig. 12, it can be found that the blade tip vortex originated and developed in upstream region ($0° < \theta < 180°$) and then weakened in downstream region ($180° < \theta < 360°$). Considering the rotation effect, the blade tip vortex mainly had influence on the front side ($0° < \theta < 180°$) in wake region. Furthermore, the detached vortex has larger area within upstream ($0° < \theta < 120°$), so that it also has significant effect on front side of wake region. The feature of this asymmetrical distribution of energy loss can be used to guide the design of wind farm configuration.

$$C_l = \frac{\int_{-1.0H}^{1.0H} f_{EPR}(z)dz}{\frac{1/2\rho A_c U_\infty^3}{V_c T} H_c} \tag{23}$$

where C_l was energy loss coefficient, $f_{EPR}(z)$ was the EPR function versus z variation, A_c was the area of inlet of computational domain, V_c was the volume of computational domain, H_c was the height of computational domain, T was the temperature.

As discussed before, the spatial distribution of energy loss in wake region from $x = 1D$ to $x = 10D$ was presented, and the conclusion of the influence of blade tip vortex on energy loss was concluded qualitatively. To further study the energy loss features in wake region in z direction quantitatively, ten control lines were set in wake region along z direction as shown in Fig. 13. Fig. 14 depicted the averaged EPR value variation within one rotational cycle on control lines from 1D to 10D. Generally,

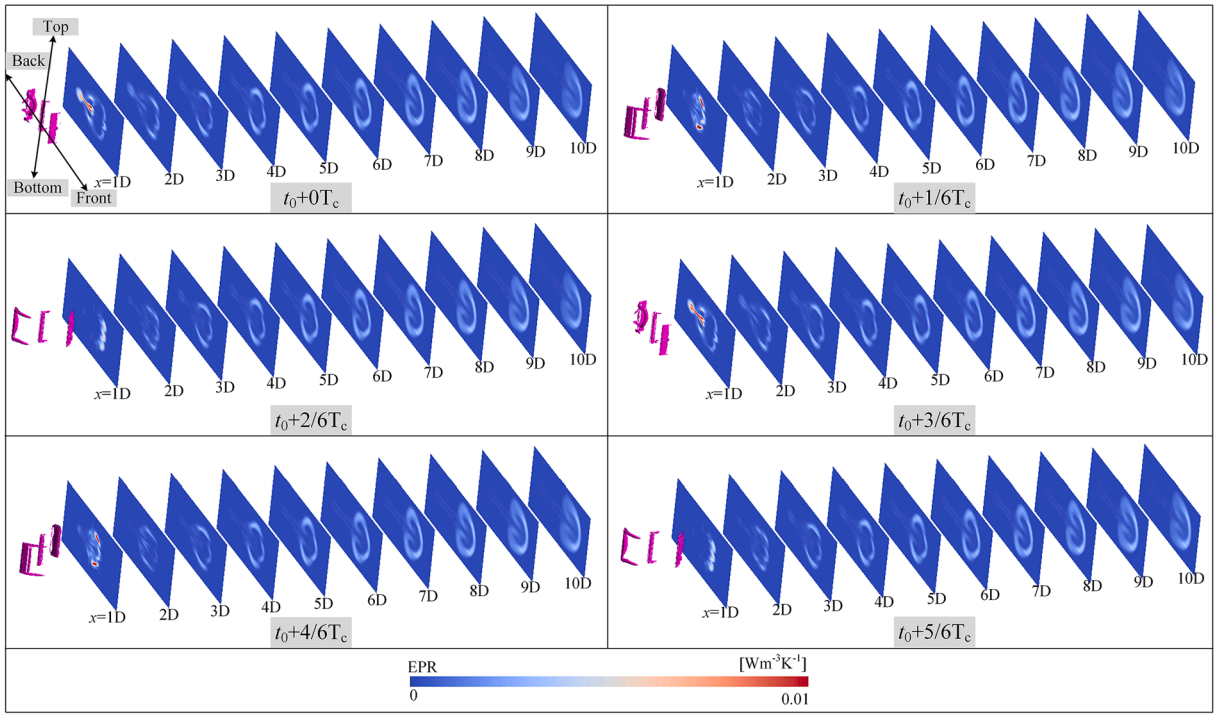

Fig. 9. The local distribution of EPR on YZ planes of wake region under $\lambda = 1.38$ condition.

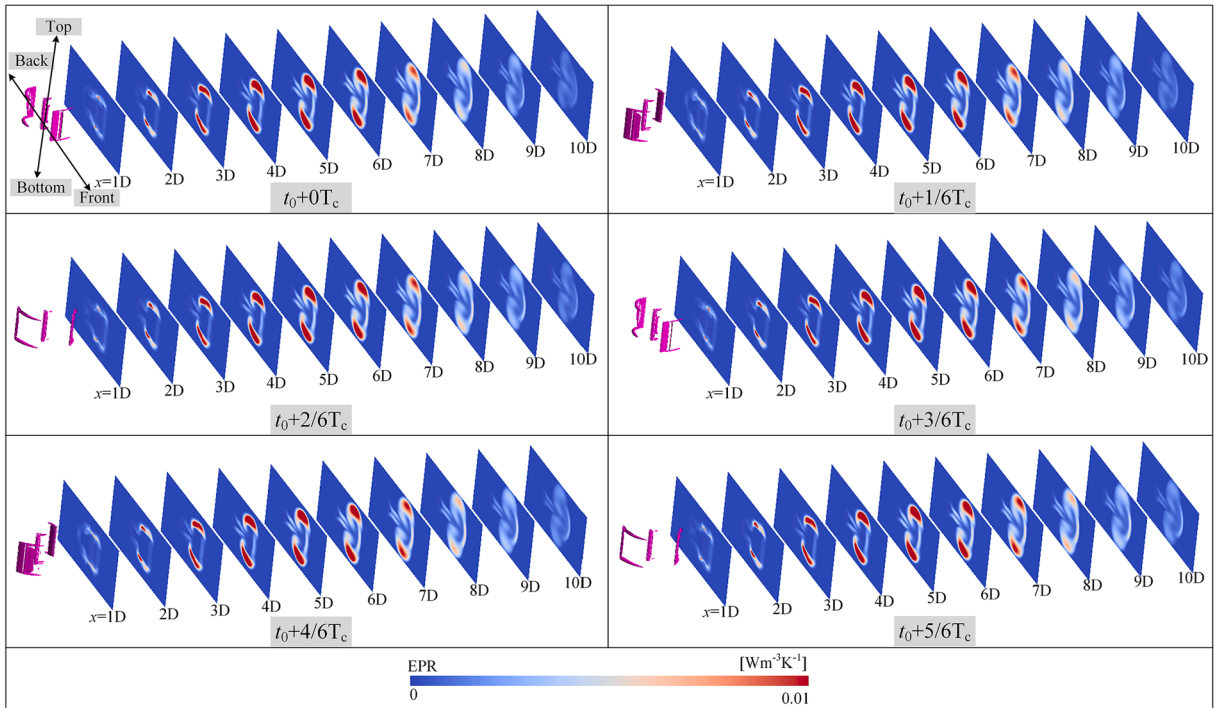

Fig. 10. The local distribution of EPR on YZ planes of wake region under $\lambda = 2.19$ condition.

the amplitude of EPR was enhanced with TSR increasing, which meant the energy loss increased with TSR increasing. Two fluctuation peaks can be observed on any control lines in Fig. 14 especially from $x = 1D$ to $x = 5D$. Owing to the recovery of kinetic energy gradually in far wake region, the features of peaks were weakened and EPR curves tended to flatness. It can be concluded that the two fluctuation peaks as well as blade tips were at the same height approximately. Therefore, it was obvious that the energy loss in wake region was mainly induced by blade tip vortex. The blade tip vortex originated from blade tips and the influence propagated downstream with main flow. Note that the amplitude as well as area of EPR curves from $x = 3D$ to $x = 5D$ were larger than EPR curves from $x = 1D$ to $x = 2D$ except $\lambda = 1.38$ condition. This was because the blade vortex diffusion under the shearing effect between main flow and tip vortex flow. In this process, the general strength of vortex was weakened and the area of vortex was enlarged. Under $\lambda = 1.38$ condition, it can be found from Fig. 6 that the flow separation on

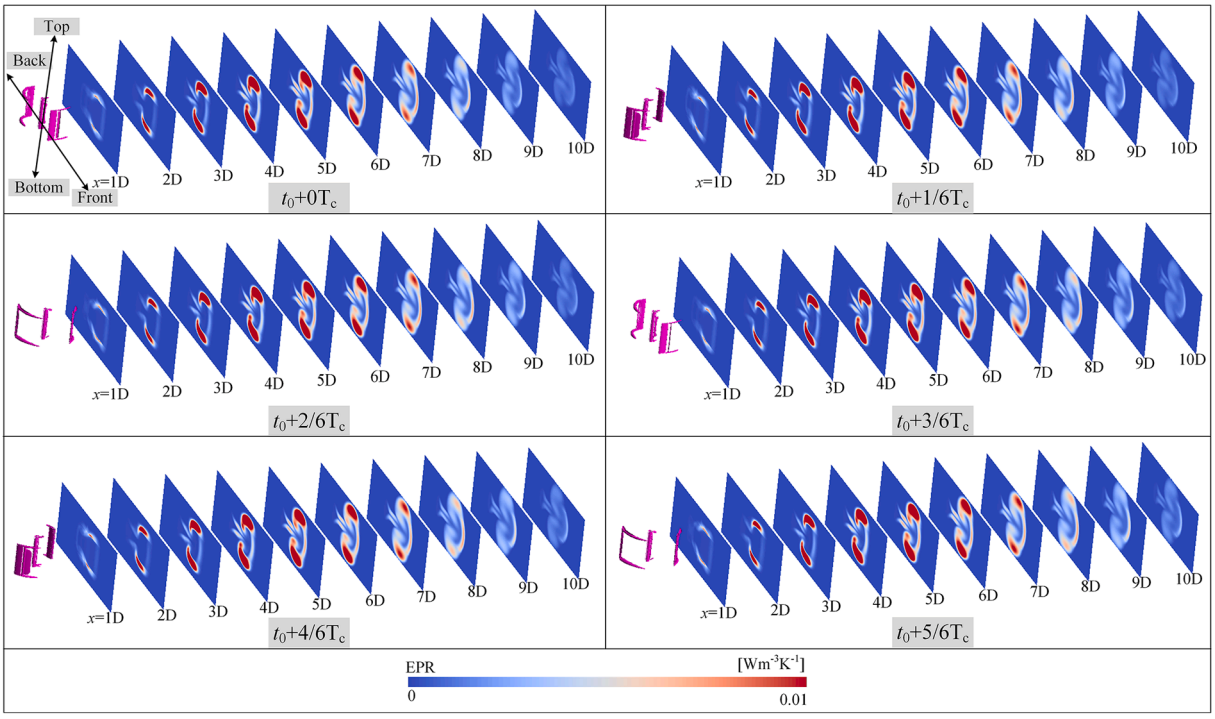

Fig. 11. The local distribution of EPR on YZ planes of wake region under $\lambda = 2.36$ condition.

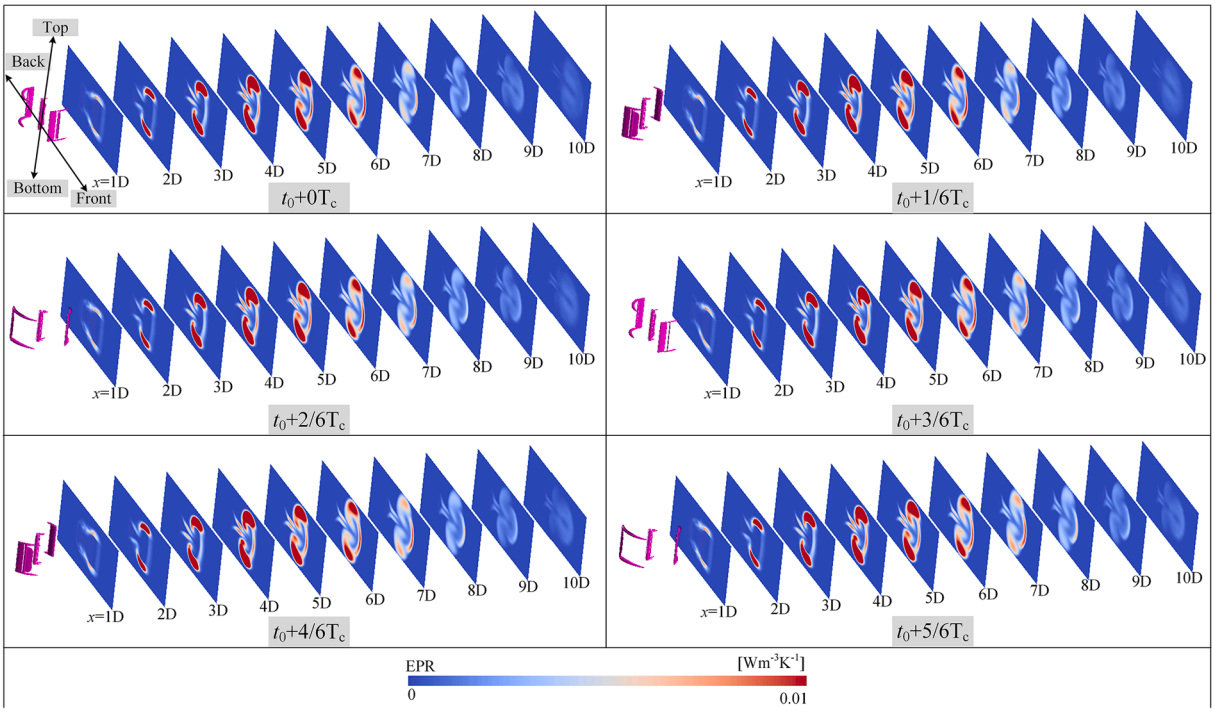

Fig. 12. The local distribution of EPR on YZ planes of wake region under $\lambda = 2.58$ condition.

suction side was severe. Combine with Fig. 9, the detached vortex as well as blade tip vortex were slighter compared with other conditions and it was not able to diffuse to downstream and it weakened downstream gradually.

To further study the energy loss quantitatively, the energy loss coefficient was defined in Eq. (23). Considering the EPR was calculated by integrating over the total computational domain, the input power was defined as the total power of inlet $1/2\rho A_c U_\infty^3$. $\int_{-1.0H}^{1.0H} f_{EPR}(z)dz$ was the integral area of EPR curves for any control lines, and the shaded area shown in Fig. 14 was the integral area, which represented the local energy loss. So that the energy loss coefficient C_l represented kinetic energy deficit, the proportion of local energy loss in input energy, and the value of C_l for any control line under four conditions were shown in Table 2. It can also be concluded that the energy loss coefficient increased with TSR increasing. Under optimal condition $\lambda = 2.19$, the energy loss coefficient C_l decreased to 0.1051 until $x = 8D$ in wake

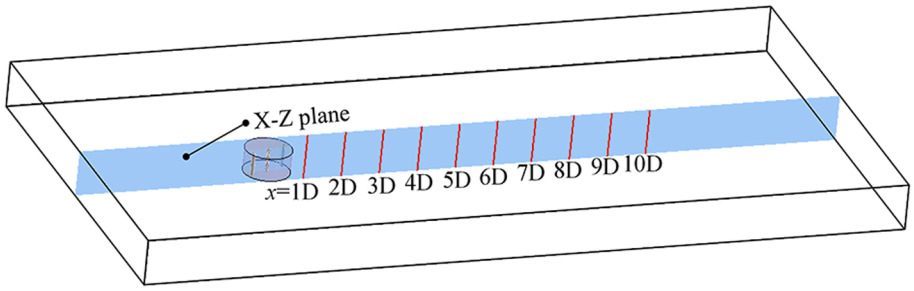

Fig. 13. The control lines along *z* direction in wake region from 1D to 10D.

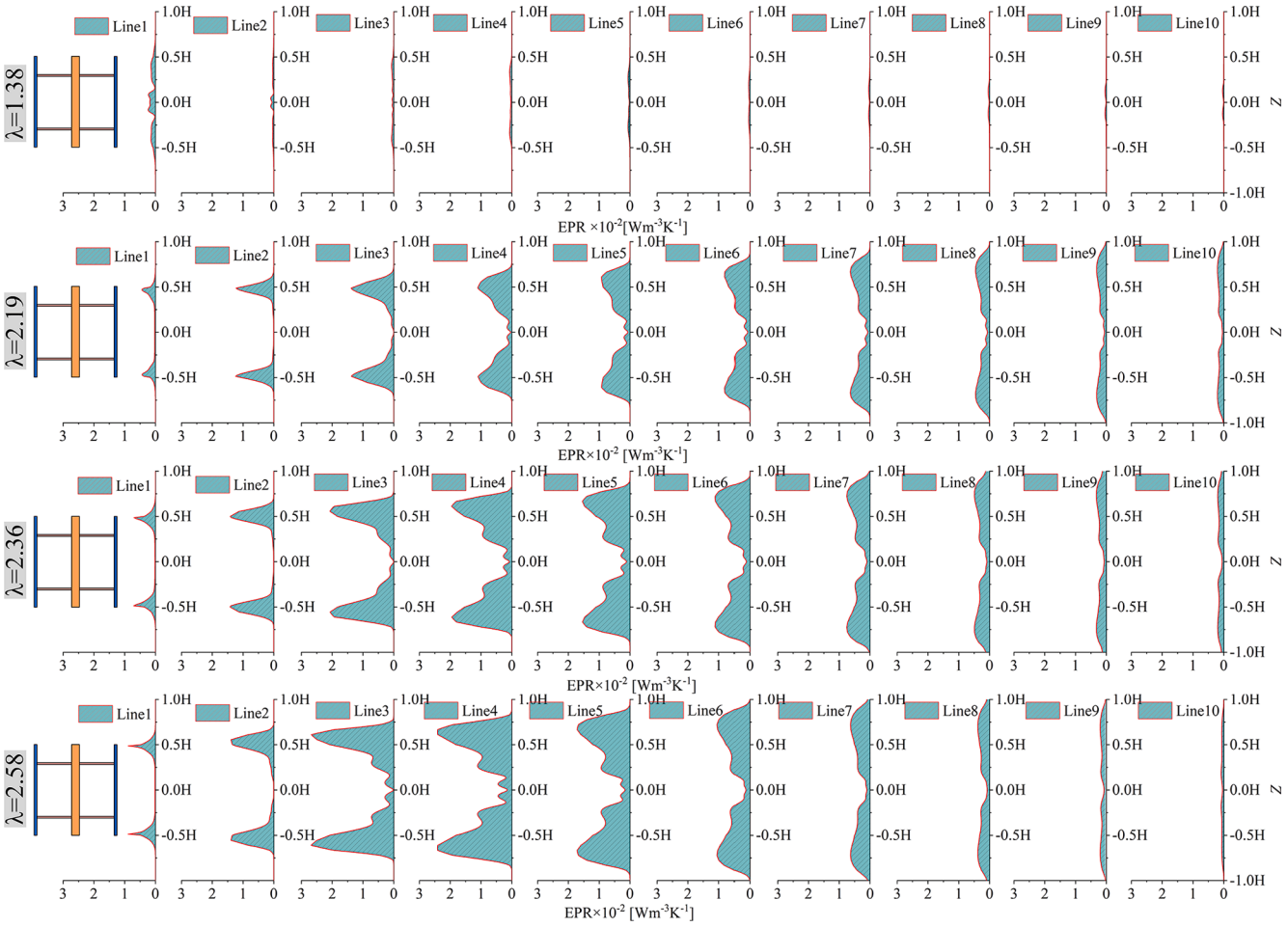

Fig. 14. The distribution of averaged EPR on control lines in wake region versus four TSR conditions.

Table 2
The energy loss coefficient from 1D to 10D under four TSR conditions.

TSR	C_l									
	x = 1D	x = 2D	x = 3D	x = 4D	x = 5D	x = 6D	x = 7D	x = 8D	x = 9D	x = 10D
1.38	0.0275	0.0085	0.0099	0.0091	0.0077	0.0051	0.0043	0.0033	0.0029	0.0024
2.19	0.0226	0.0623	0.1182	0.1525	0.1596	0.1528	0.1330	0.1051	0.0784	0.0561
2.36	0.0306	0.0933	0.2240	0.2937	0.2790	0.2331	0.1765	0.1262	0.0884	0.0593
2.58	0.0311	0.1108	0.3057	0.3901	0.3356	0.2401	0.1620	0.1051	0.0590	0.0225

region. Generally, the energy loss coefficient reduced to 0.1 between 8D to 9D except for $\lambda = 1.38$ condition. Owing to the low power coefficient, the maximum energy loss coefficient was 0.0275 at x = 1D under λ = 1.38 condition. Therefore, the defined energy loss coefficient can reflect the energy deficit as well as kinetic energy recovery in wake region quantitatively and reflect what and where energy loss intuitively. The energy loss coefficient C_l can be used to guide the configuration optimization of VAWTs to improve the wind energy utilization as well as

revenue of wind farms.

5. Conclusions

In this study, the energy loss characteristics of an H-type VAWT were conducted by numerical simulation method under four TSR conditions. The simulation was carried out under optimum blade pitch angle $\beta = 6^{\circ}$ and the maximum power coefficient appeared on TSR = 2.19 condition. The entropy production theory was introduced to calculate energy loss in VAWTs flows versus various TSR conditions quantitatively. The energy loss in runner was analyzed and the spatial distribution of energy loss in wake region was revealed. The main conclusions can be drawn as follows:

(1) The local vorticity field around blades indicated that the flow regimes varied from flow separation to attached flow with TSR increasing. The EPDD was the dominant variable reflecting how and where the TEPR varies. The minimum TEPR can be set as the objective function to calculate optimum TSR of VAWTs and promote the development of wind power.
(2) The blade tip vortex was the dominant factor to induce energy loss in wake region and two fluctuation peaks of EPR curves appeared at blade tips $z = 0.5$H as well as $z = -0.5$H. Under low TSR $\lambda = 1.38$ condition, the energy utilization and deficit were lower than other conditions. The distribution of EPR in wake region was asymmetrical and the high-level EPR was distributed on front side in wake region due to the influence of blade tip vortex. The features of asymmetrical distribution can be used to determine the distance for stagger arrangement VAWTs.
(3) The energy loss coefficient was defined to represent the extent of energy deficit as well as the proportion of energy loss in total input energy. Generally, the energy loss coefficient reduced to 0.1 between $x = 8$D to $x = 9$D in wake region. And the energy loss was equal to 0.1051 at $x = 8$D under optimal condition $\lambda = 2.19$. The energy loss coefficient can reflect what and where energy deficit and kinetic energy recovery and it can guide configuration optimization of wind farms.

CRediT authorship contribution statement

Qinghong Tang: Software, Validation, Formal analysis, Data curation, Writing – original draft, Visualization. **Yuxin Wu:** Writing – review & editing, Supervision, Funding acquisition. **An Yu:** Writing – review & editing, Funding acquisition. **Bin Peng:** Resources. **Yifu Wang:** Resources. **Junfu Lyu:** Writing – review & editing, Resources.

Declaration of Competing Interest

The authors declare that they have no known competing financial interests or personal relationships that could have appeared to influence the work reported in this paper.

Data availability

The authors do not have permission to share data.

Acknowledgments

This research was funded by the Fundamental Research Funds for the Central Universities (2022ZFJH004) , Seed fund of Shanxi Research Institute for Clean Energy, Tsinghua University, the National Natural Science Foundation of China (Project No. 52276029).

References

[1] Hashim IJ. A New Renewable Energy Index. In: 2021 6th International Conference on Renewable Energy: Generation and Applications; (ICREGA)2021.. p. 229–32.
[2] Li Q, Maeda T, Kamada Y, Murata J, Shimizu K, Ogasawara T, et al. Effect of solidity on aerodynamic forces around straight-bladed vertical axis wind turbine by wind tunnel experiments (depending on number of blades). Renewable Energy 2016;96:928–39.
[3] Li Q, Maeda T, Kamada Y, Murata J, Yamamoto M, Ogasawara T, et al. Study on power performance for straight-bladed vertical axis wind turbine by field and wind tunnel test. Renew Energy 2016;90:291–300.
[4] Zamani M, Sangtarash A, Javad Maghrebi M. Numerical Study of Porous Media Effect on the Blade Surface of Vertical Axis Wind Turbine for Enhancement of Aerodynamic Performance. Energ Conver Manage 2021;245:114598.
[5] Arpino F, Cortellessa G, Scungio M, Fresilli G, Facci A, Frattolillo A. PIV measurements over a double bladed Darrieus-type vertical axis wind turbine: A validation benchmark. Flow Meas Instrum 2021;82:102064.
[6] Miao W, Liu Q, Xu Z, Yue M, Li C, Zhang W. A comprehensive analysis of blade tip for vertical axis wind turbine: Aerodynamics and the tip loss effect. Energ Conver Manage 2022;253:115140.
[7] Somoano M, Huera-Huarte FJ. Bio-inspired blades with local trailing edge flexibility increase the efficiency of vertical axis wind turbines. Energy Rep 2022;8:3244–50.
[8] Hao W, Bashir M, Li C, Sun C. Flow control for high-solidity vertical axis wind turbine based on adaptive flap. Energ Conver Manage 2021;249:114845.
[9] Chen W-H, Wang J-S, Chang M-H, Tuan Hoang A, Shiung Lam S, Kwon EE, et al. Optimization of a vertical axis wind turbine with a deflector under unsteady wind conditions via Taguchi and neural network applications. Energ Conver Manage 2022;254:115209.
[10] Zhang Y, Guo Z, Zhu X, Li Y, Song X, Cai C, et al. Investigation of aerodynamic forces and flow field of an H-type vertical axis wind turbine based on bionic airfoil. Energy 2022;242:122999.
[11] Zhu X, Guo Z, Zhang Y, Song X, Cai C, Kamada Y, et al. Numerical study of aerodynamic characteristics on a straight-bladed vertical axis wind turbine with bionic blades. Energy 2022;239:122453.
[12] Li Q, Maeda T, Kamada Y, Murata J, Furukawa K, Yamamoto M. Effect of number of blades on aerodynamic forces on a straight-bladed Vertical Axis Wind Turbine. Energy 2015;90:784–95.
[13] Li Q, Maeda T, Kamada Y, Murata J, Kawabata T, Kogaki T. Study on flow around straight-bladed vertical axis wind turbine under low tip speed ratio. J Fluid Sci Technol 2014;9(3):JFST0051–.
[14] Zhang Y, Li Q, Zhu X, Song X, Cai C, Guo Z. Wind Tunnel Experiments and Numerical Study on Performance Characteristics of an H-type Vertical Axis Wind Turbine in the Spanwise Direction. J Therm Sci 2021;30(3):758–71.
[15] Mamouri AR, Khoshnevis AB, Lakzian E. Entropy generation analysis of S825, S822, and SD7062 offshore wind turbine airfoil geometries. Ocean Eng 2019;173:700–15.
[16] Mamouri A, Lakzian E, Bak Khoshnevis A. Entropy analysis of pitching airfoil for offshore wind turbines in the dynamic stall condition. Ocean Eng 2019;187:106229.
[17] Soltanmohamadi R, Lakzian E. Improved Design of Wells Turbine for Wave Energy Conversion Using Entropy Generation. Meccanica 2016;51:1713–22.
[18] Nazeryan M, Lakzian E. Detailed entropy generation analysis of a Wells turbine using the variation of the blade thickness. Energy 2018;143:385–405.
[19] Ghisu T, Cambuli F, Puddu P, Mandas N, Seshadri P, Parks G. Numerical Evaluation of Entropy Generation in Isolated Airfoils and Wells Turbines. Meccanica 2018;53:3437–56.
[20] Herwig H, Fabian K. Direct and indirect methods of calculating entropy generation rates in turbulent convective heat transfer problems. Heat Mass Transf 2006;43:207–15.
[21] Kock F, Herwig H. Local entropy production in turbulent shear flows: a high-Reynolds number model with wall functions. Int J Heat Mass Transf 2004;47(10-11):2205–15.
[22] Li D, Wang H, Qin Y, Han L, Wei X, Qin D. Entropy production analysis of hysteresis characteristic of a pump-turbine model. Energ Conver Manage 2017;149:175–91.
[23] Wilcox D. Reassessment of the scale-determining equation for advanced turbulence models. AIAA J 1988;26:1299–310.
[24] Menter F. Zonal Two Equation k-w Turbulence Models For Aerodynamic Flows. AIAA Paper 1993;1993.
[25] Lu D, Xiaolin W, Zhongli J, Zhiyi X, Jingxian Z. The flow pattern and entropy generation in an axial inlet cyclone with reflux cone and gaps in the vortex finder. Powder Technol 2016;303:192–202.
[26] Lu D, Xiaolin W, Zhongli J, Qixian F. Entropy generation analysis on cyclone separators with different exit pipe diameters and inlet dimensions. Chem Eng Sci 2015;138:622–33.
[27] Lei H, Zhou D, Bao Y, Li Y, Han Z. Three-dimensional Improved Delayed Detached Eddy Simulation of a two-bladed vertical axis wind turbine. Energ Conver Manage 2017;133:235–48.